

Effects of Aging at 450°C on the Pitting Corrosion Resistance and Toughness of AISI 317L Steel Welded by GTAW and FSW

Humberto Nogueira Farnetze^{a*}, Sérgio Souto Maior Tavares^b, Juan Manuel Parda^b,

Cássio Barbosa^c, Olívia Cypreste Pereira^c, Rachel Pereira Carneiro da Cunha^c

^aCentro Federal de Educação Tecnológica, Unidade Itaguaí (CEFET/RJ), CEP 23810-000, Itaguaí, RJ, Brazil

^bDepartamento de Engenharia Mecânica, Universidade Federal Fluminense (UFF), CEP 24210-240, Niterói, RJ, Brazil

^cInstituto Nacional de Tecnologia (INT), CEP 20081-312, Rio de Janeiro, RJ, Brazil

Received: December 12, 2016; Revised: September 18, 2017; Accepted: October 13, 2017

Austenitic stainless steels are high corrosion resistant alloys widely used in many industrial fields. Among this family of steels, AISI 317L stands out due to its higher localized corrosion resistance when compared to the traditional grades AISI 304L and AISI 316L. In some applications in oil refineries, the AISI 317L is being specified for services at moderately high temperatures. At the same time as it is sought to use new stainless steels, is also desirable to apply and develop emerging welding processes, replacing conventional ones, in order to achieve better behavior in service. In this respect, this work studied the effects of thermal aging on the toughness and resistance to pitting corrosion of AISI 317L steel weld metals produced by the Gas Tungsten Arc Welding (GTAW) and Friction Stir Welding (FSW) joining processes. After prolonged exposures at 450°C, for 200h, 300h and 400h, the microstructural characterization by scanning electron microscopy (SEM), toughness evaluation and anodic polarization tests in 3.5% NaCl solution were performed. The results showed that the increase of the exposure time in both weld metals caused a toughness decrease. The pitting potentials measured in the polarization tests also decreased with the aging at 450°C.

Keywords: AISI 317L, GTAW, FSW, toughness, pitting corrosion

1. Introduction

Austenitic stainless steels are high corrosion resistant alloys with excellent mechanical properties, mainly toughness at low temperatures. In this family, AISI 317L steel stands out due to its higher resistance to localized corrosion when compared to the traditional grades AISI 304L and AISI 316L^{1,2}.

Several installations in the refineries are subjected to aggressive and corrosive environment of petroleum and its derivatives. It includes services with solutions containing chlorides, sulfates, sulfur solutions, hydrocarbon compounds, nitrogenated and oxydizing environments.

Corrosion leads to increased equipment maintenance costs and it is necessary to use materials that, in addition to having good toughness and strength to withstand high pressures in temperatures above the environment, must be corrosion resistant. Therefore, austenitic stainless steels can be selected to both transport and processing part of such corrosive fluids^{3,4}.

At the same time as it is sought to use new stainless steels, it seeks to apply and develop emerging welding processes, replacing conventional ones, to obtain better

behavior in service. In conventional welding the process temperature exceeds the melting temperature of the materials. In this way, the union of austenitic stainless steels presents distortion problems, caused by the thermal expansion and dissipation of the materials. In addition, the presence of pores, solidification cracks, residual stress, precipitation of $M_{23}C_6$ carbide and intermetallic phases σ and χ increases the susceptibility of the welded joint to corrosion and embrittlement⁴⁻⁶. All these problems raise the maintenance costs, as well as increases the thickness of the steels to withstand the aggressive fluid and still maintain the mechanical resistance to withstand the high process pressures in welded joints.

Austenitic stainless steels are widely used in the petrochemical industry and joining of these steels by friction stir welding (FSW) can lead to cost reduction and help in the design of intelligent projects. Despite being a consolidated process for aluminum and its alloys, and being a process with increasing use in steels, few scientific articles were published with the FSW process applied to austenitic stainless steels. In this context, this work investigated the aspects involving changes in metallurgical behavior of AISI 317L stainless steel, when welded by conventional arc welding and solid state welding FSW.

*e-mail: humbertofarnetze@gmail.com

2. Experimental Procedures

The welded joints were made using AISI 317L stainless steel plates, with dimensions 296 mm x 116 mm x 8.0 mm by GTAW, and dimensions 655 mm x 100 mm x 6.35 mm by FSW. Tables 1 and 2 show the chemical compositions of the base metal and feed metal (AWS A 5.9 ER 317L rod). These chemical analyses were carried out by combustion method (C, N and S) and Atomic Emission Spectrometry by spark (other elements).

Manual GTAW process was performed with a qualified welder. Figure 1 shows the dimension and details of the joint geometry used, following the recommendations of AWS C 5.5-80⁷. The multipass welding was performed in flat position with a maximum interpass temperature of 150 °C, using Argon with 99.99% purity as protection gas. The welding parameters are shown in Table 3.

The welded joint FSW was produced in the machine TTI RM-2 (Transformation Technologies Inc.) from the Brazilian Nanotechnology National Laboratory. The welding tool was composed by PCBN (Polycrystalline Cubic Boron Nitride) (60%vol.) and W-Re alloy (40%vol.).

Welding parameters are presented in Table 4. The average welding energy (E_w) was calculated from Equations 1 and 2 shown below:

$$C_R = \frac{\Delta W}{\lambda \cdot l} \quad (1)$$

$$\eta_{wz} = \left(1 - \frac{C_w}{C_b}\right) \times 100 \quad (2)$$

Where P is the power of the process (kW), v is the forward speed of the tool (mm/s), Ω the rotation speed of the tool (rpm), and T the average torque recorded in the process (N.m)⁸.

After welding, specimens from the welded joint and base metal were aged at 450 °C for 200 h, 300 h and 400 h, with subsequent water cooling.

The microstructures of the weld metals (WM) were analyzed by optical microscopy (OM), scanning electron microscopy (SEM) and X-ray dispersive energy (EDS)

Table 1. Chemical composition of the base metal (wt%). (Fe) balance.

Material	C	Mn	Si	S	P	Cr	Ni	Mo	Fe
AISI 317L	0.024	1.34	0.47	0.003	0.031	18.13	11.41	3.02	Bal.

Table 2. Chemical composition of the rod GTAW (wt%). (Fe) balance.

Feed metal	C	Mn	Si	S	P	Cr	Ni	Mo	Fe
AWS A 5.9 ER 317L	0.008	1.75	0.56	0.002	0.024	19.1	14.1	3.19	Bal.

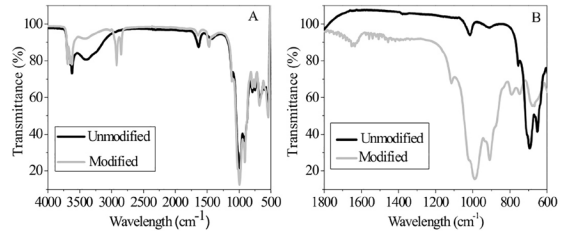


Figure 1. Details of welded joint geometry. Dimensions in mm.

spectroscopy. To reveal the microstructural characteristics, the chemical attack with the Behara's reagent (20ml HCl + 80 ml H₂O + 0.3g potassium metabissulfite) was used.

Electron backscattered scanning diffraction (EBSD) was used to identify the phases precipitated in the samples of weld metals un-aged. For this analysis a Field Emission Gun Scanning Electron Microscope (FEG-SEM) FEI QUANTA 400 was used. The specimens were gingerly polished with colloidal silica.

Magnetic analysis with ferritoscope Helmut Fischer[®] was used to measure the delta ferrite content. Thermocalc[®] simulation with TCFE6 data base was used to predict the phases more stable at 450 °C.

Transversal sub-size specimens (5 mm) for Charpy impact tests were machined the welded joints. The V notch was placed in the center line of the weld metal. Impact tests were carried out at room temperature in an universal machine with 300J of capacity.

Cyclic polarization tests in 3.5% NaCl solution were used to evaluate the pitting corrosion resistance, as detailed described in the ASTM G-61 standard⁹. A three electrodes cell, with working electrode of the material analyzed, reference and counter-electrode were used. Working electrodes were prepared with the specimen to be analyzed embedded in epoxy resin among with a cooper wire for electric contact. Saturated calomel electrode was used as reference and a Pt wire was used as counter-electrode. The tests were conducted with the solution at 22 °C. After the stabilization of the open circuit potential (E_{OC}) the anodic polarization with sweep rate 1 mV/s initiated. The sweeping was reverted to the cathodic direction when the current density achieved 1mA/cm².

Table 3. Welding parameters and average welding energy.

Process	Φ (mm)	Polarity	Current (A)	Voltage (V)	E_w (kJ/mm)	N° Passes
GTAW	2.4	CC-	112 - 150	9 - 10	1.04 ± 0.24	7

Φ – diameter of the welding rod; E_w – welding energy.

Table 4. FSW parameters and average welding energy.

FSW Process	
Penetration (%)	93.3
Speed of Advance, v (mm/min)	100
Rotation Speed, Ω (rpm)	364
Average Torque, T (N.m)	81
E_w (kJ/mm)	1.8

3. Results and Discussion

Table 5 shows the chemical compositions of weld metals, and the Cr_{eq} and Ni_{eq} calculated using the equations from the WRC-92 diagram for microstructure prediction ($Cr_{eq} = \%Cr + \%Mo + 0.7(\%Nb)$ and $Ni_{eq} = \%Ni + 35(\%C) + 20(\%N) + 0.25(\%Cu)$)¹⁰. The Cr, Ni, Mo and C contents were used as input to Thermocalc® simulation. Figure 2 shows the results for weld metals. Table 6 shows the equilibrium volume fractions of ferrite (δ), sigma (σ), chi (χ) and $M_{23}C_6$ in weld metals calculated with Thermocalc®.

Figures 3 (a) and (b) show the macrographic appearance of the joints welded by the GTAW and FSW processes, respectively. The visual inspection of the macrographic section did not detect any metallurgical defect.

Figures 4 (a) and (b) show the microstructural features observed by SEM in as welded GTAW and FSW weld metals, respectively. Tables 7 and 8 show the chemical compositions

determined by EDS from the reference points indicated in Figures 4 (a) and (b), respectively.

SEM images show the phases austenite (γ) (point 1 in Figures 4(a) and (b)) and ferrite (δ) (point 2 in the same Figures). The microstructural analysis reveals the presence of intermetallic phases (IP) formed in the interface δ/γ (point 3 in Figure 4(a)), as well as inside ferrite (δ) (point 4 in Figure 4(a) and point 3 in Figure 4(b)). Tables 7 and 8 show the EDS analyses of selected points of Figures 4(a) and 4(b), respectively. One can observe that the ferritizing elements Cr and Mo are more concentrated in the ferrite phase, while austenitizing elements Ni and Mn are more concentrated in the austenite phase. Even being a semi-quantitative analysis, EDS is helpful to identify intermetallic phases. Points 3 and 4 of Figure 4(a) and point 3 of Figure 4(b) have higher Mo content than the ferrite phase. These regions may correspond to chi (χ) or sigma (σ) phases.

It can be assumed that the presence of deleterious intermetallic phases in the GTAW weld metal, as welded, is a result of the chemical composition and the effects of the additional thermal cycling on multipass welding.

The research developed by Song et al.¹¹, using transmission microscopy (TEM), detected the presence of the chi (χ) phase at the δ/γ interface, in an AISI 317L steel welding metal produced by multipass welding to the electric arc and without further thermal aging. It is important to

Table 5. Chemical composition of the weld metals (WM) of GTAW and FSW (wt%).

WM	C	Mn	Si	S	P	Cr	Ni	Mo	Fe	Cr_{eq}	Ni_{eq}
GTAW	0.008	1.63	0.61	0.003	0.028	18.26	13.63	3.08	Bal.	21.3	13.9
FSW	0.030	1.52	0.29	0.003	0.030	18.02	11.14	3.04	Bal.	21.1	12.0

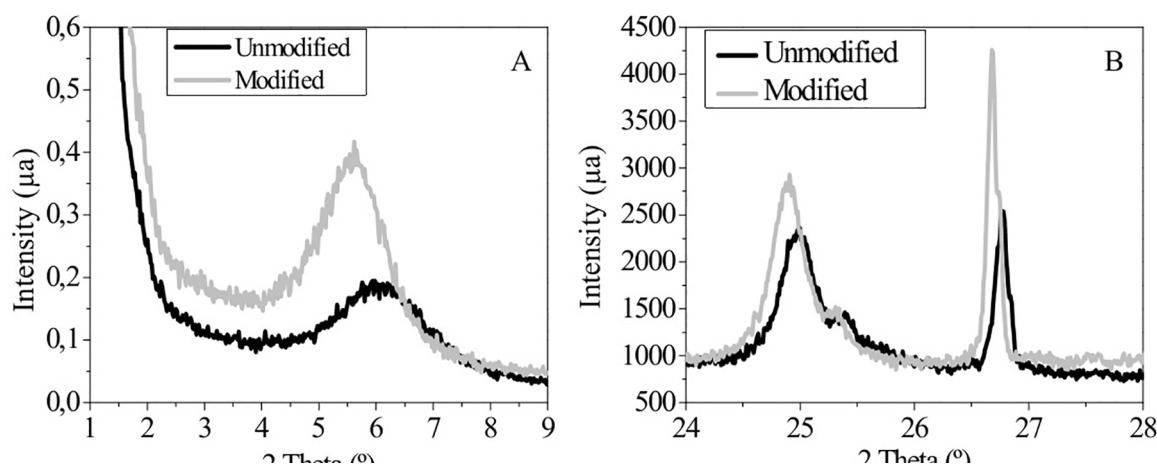
**Figure 2.** Equilibrium phase volume fractions as function of temperature determined by computational thermodynamics: (a) GTAW; (b) FSW

Table 6. Phase composition and volume fraction predictions from Thermocalc® to weld metals aged at 450 °C.

Weld Metal	Volume Fraction in Equilibrium – 450°C			
	Ferrite (δ)	Sigma (σ)	Chi (χ)	$M_{23}C_6$
GTAW	0.4388	0.2241	-----	0.0023
FSW	0.5335	0.2108	-----	0.0067

consider that the weld metal analyzed by these researchers presented the content of 3.6% Mo, increasing the possibility of precipitation of this phase, which is directly linked to the content of this element in the alloy. The studies of Park et al.¹² and Kokawa et al.¹³, also using MET analysis, suggest the presence of sigma phase (σ) in AISI 304 steel welded

by FSW. Analyzing the same welding process, Chen et al.¹⁴ also observed the sigma phase (σ) in AISI 316L steel. The work of these researchers suggests that large deformation and recrystallization also contributes to the precipitation of sigma phase (σ) in the microstructure consisting of ferrite (δ) and austenite (γ).

The analyses, by EBSD, of the un-aged GTAW and FSW weld metals are presented in Figures 5 (a) and (b), respectively. The results also point to the presence of intermetallic phases, converging to the aspects observed in Figures 4 (a) and (b). Tables 9 and 10 provide the identification and quantification of these intermetallic phases, indicating that in addition to the sigma phase (σ), it can also be observed chi (χ) and $M_{23}C_6$ phases in the microstructure of the un-aged weld metals.

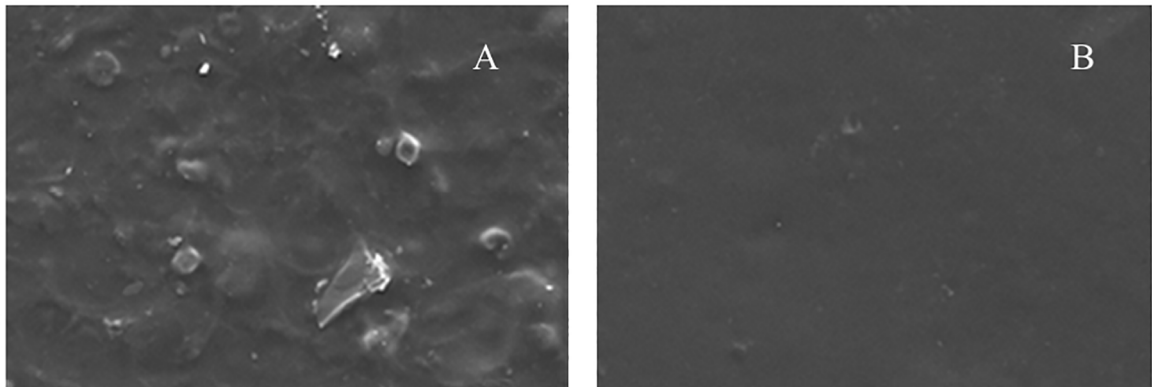


Figure 3. Macroscopic aspect of welded joints. (a) GTAW. (b) FSW.

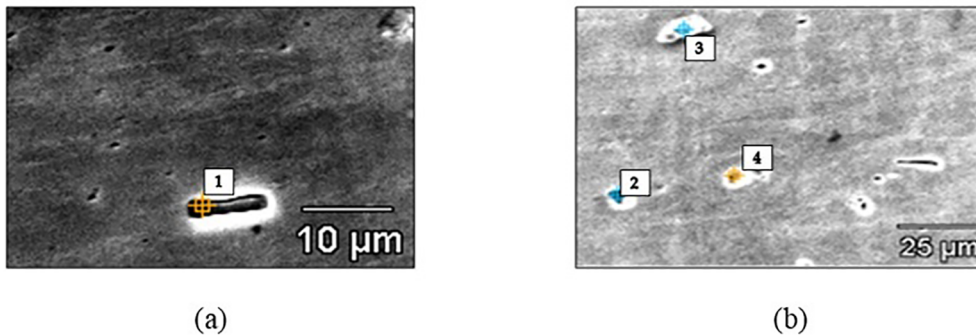


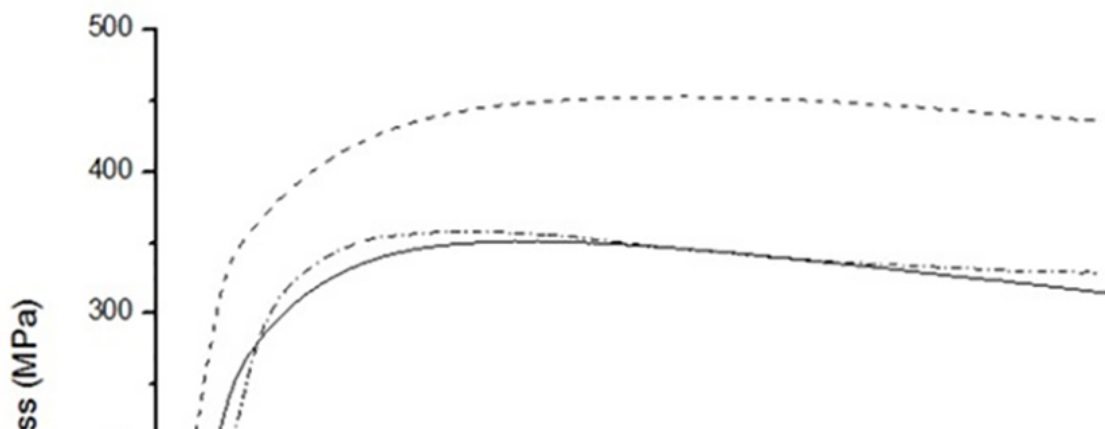
Figure 4. Microstructural aspect of weld metals in the condition as welded. (a) GTAW; (b) FSW. Behara's etching.

Table 7. Semi-quantitative chemical analysis determined by EDS of points identified by arrows in Figure 4(a) (wt%).

Points	Cr	Ni	Mo	Mn	Si	Fe	Phase
1	18.63	14.74	3.56	1.47	1.02	Bal.	γ
2	23.57	7.52	4.10	1.28	0.78	Bal.	δ
3	19.91	10.98	5.63	1.12	1.28	Bal.	IP
4	19.94	10.93	5.72	1.63	0.90	Bal.	IP

Table 8. Semi-quantitative chemical analysis determined by EDS of points identified by arrows in Figure 4(b) (wt%).

Points	Cr	Ni	Mo	Mn	Si	Fe	Phase
1	18.81	11.06	3.40	1.49	0.79	Bal.	γ
2	19.10	9.98	4.85	1.08	0.71	Bal.	δ
3	21.19	7.96	5.20	1.02	0.95	Bal.	IP

**Figure 5.** Phase maps obtained by EBSD in un-aged weld metals: (a) GTAW. (b) FSW**Table 9.** Amounts of phases determined by EBSD in the weld metal GTAW.

Phase	Volume Fraction
γ	0.878
δ	0.065
σ	0.011
χ	0.007
$M_{23}C_6$	0.013

Table 10. Amounts of phases determined by EBSD in the weld metal FSW.

Phase	Volume Fraction
γ	0.826
δ	0.036
σ	0.008
χ	0.012
$M_{23}C_6$	0.038

Table 11. Semi-quantitative chemical analysis determined by EDS of points selected in Figure 6(a) (wt%). (%Fe = balance).

Points	Cr	Ni	Mo	Mn	Si	Phase
1	18.55	13.54	3.50	1.87	0.69	γ
2	22.58	8.14	4.82	1.73	0.54	δ
3	19.32	11.26	5.09	1.73	1.23	IP
4	20.21	10.88	4.95	1.62	0.85	IP

Figures 6(a) and (b) show the microstructural aspect, observed by scanning electron microscopy (SEM), of samples of GTAW and FSW weld metals aged for 400 hours, respectively. The chemical compositions by EDS, from selected points indicated in Figures 6(a) and 6(b), are shown in Tables 11 and 12, respectively. In the weld metals, an increase in the intermetallic phase (IP) precipitation inside the ferrite (δ) (points 3 of Figures 6 (a) and (b)) is observed, as well as the presence of a massive phase in the δ/γ interface in the GTAW weld metal (point 4 of Figure 6 (a)). Chun et al.⁶, in a recent research, using AISI 316FR steel weld metals aged at 600 °C for 100h, concluded by EBSD that the finer precipitates in the ferrite (δ) correspond to chi (χ) phase and the more massive corresponds to sigma phase (σ).

In order to evaluate the effects of dynamic recrystallization on the FSW weld metal, the mean austenite (γ) grain sizes were determined by applying the ASTM E-112 intercepts method¹⁵. The results are shown in Table 13. It is possible

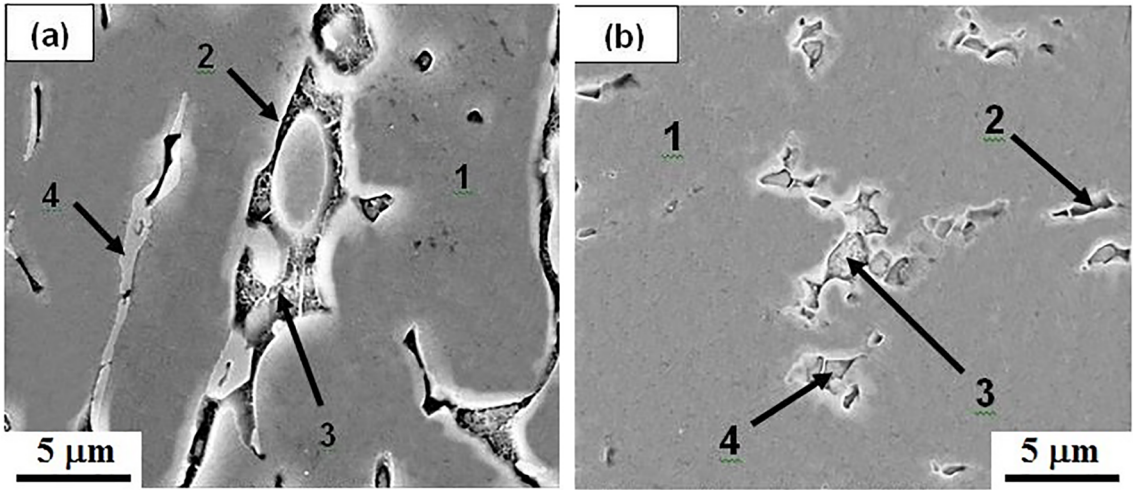


Figure 6. Images obtained by MEV from the microstructure of the thermally aged weld metals for 400 h. (a) GTAW, (b) FSW. Behara's etching.

Table 12. Semi-quantitative chemical analysis determined by EDS of points selected of Figure 6(b) (% em peso). (%Fe = balance).

Points	Cr	Ni	Mo	Mn	Si	Phase
1	18.00	11.05	3.14	1.35	0.58	γ
2	19.76	9.21	4.38	1.23	0.55	δ
3	20.39	7.97	5.42	0.95	1.10	IP
4	19.99	8.58	4.83	1.21	0.69	δ

Table 13. Grain sizes calculated by the method of the intercepts, with images obtained by OM.

Region	Grain Sizes (μm)
Base Metal	24.00
Weld Metal FSW	5.44

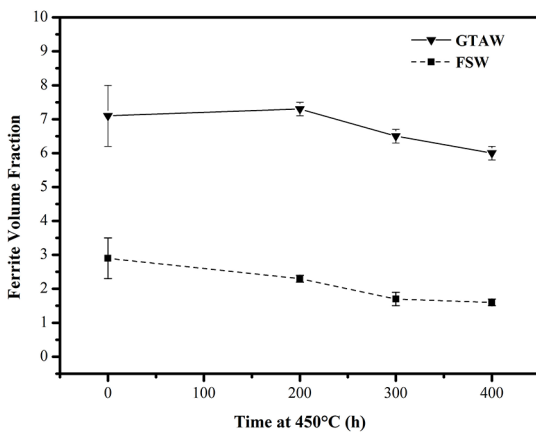


Figure 7. Variation of ferrite volume fraction with time of exposure at 450°C.

to verify that the average size of the austenite grains in the FSW weld metal is considerably smaller when compared to the base metal.

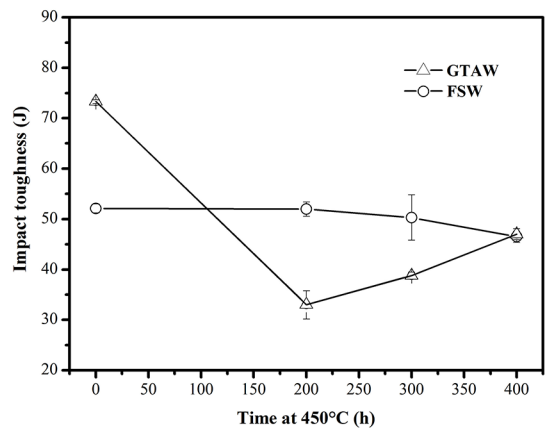


Figure 8. Variation of the impact toughness with aging time at 450 °C.

Figure 7 shows the variation of ferrite contents of the weld metals. It is worth noting that the δ ferrite volume fractions measured by ferritoscope are significantly lower than the equilibrium values found by Thermocalc analyses, which shows that the thermodynamics predictions were not observed in practice, in this case. Nevertheless, the ferrite fraction measured by ferritoscope in the WM-GTAW specimen (7.0%) is very similar to the value predicted by the WRC-92 diagram using the Cr_{eq} and Ni_{eq} calculated in Table 5¹⁰. This is a practical diagram constructed with experimental data largely used in fusion welding studies. However, the

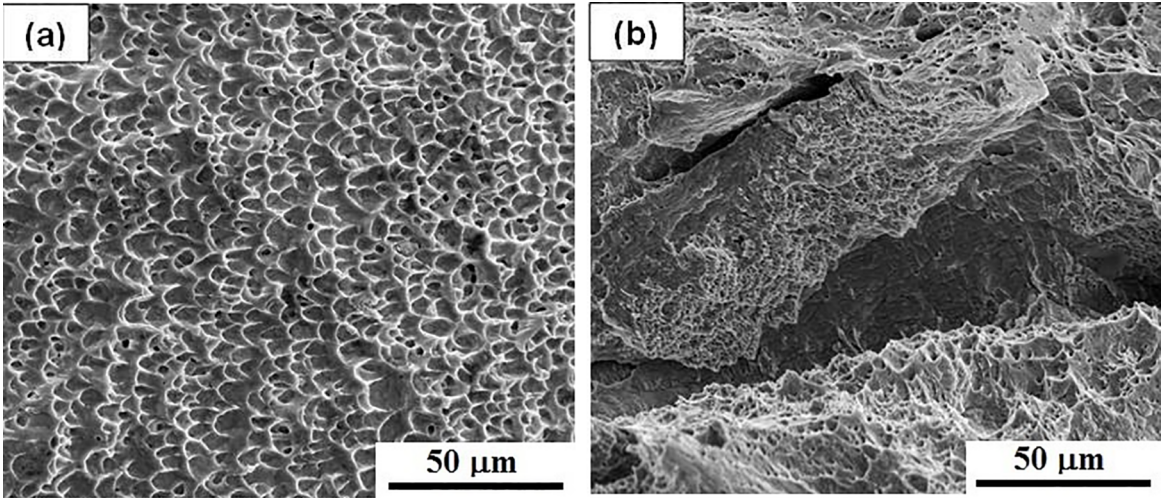


Figure 9. Surface of weld metal fracture as welded. (a) GTAW, (b) FSW.

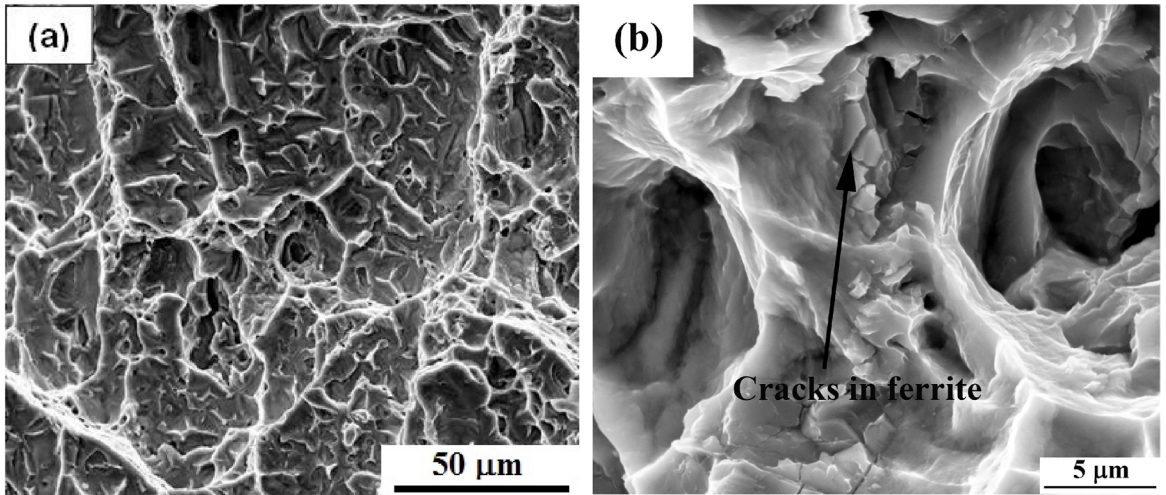


Figure 10. Surface of weld metal fracture GTAW aged for 200 h.

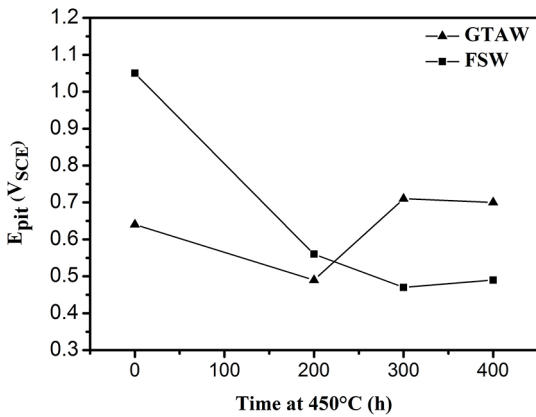


Figure 11. Pitting potential curves obtained by cyclic potentiodynamic tests.

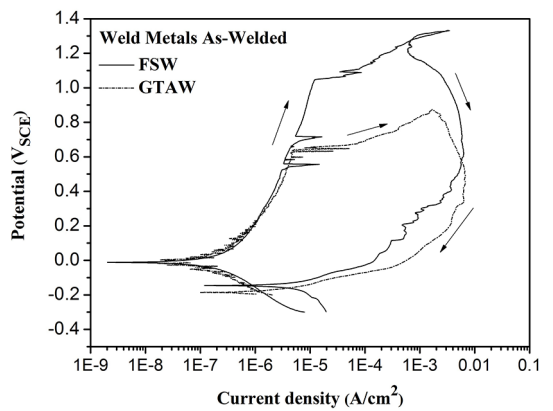


Figure 12. Polarization curves of un-aged FSW and GTAW specimens.

prediction of WRC-92 to the delta ferrite of un-aged FSW was 13.0%, while the value obtained by ferritoscope was only 3.0%. It suggests that the microstructure of solid state FSW welds cannot be predicted by the WRC-92 diagram.

In both weld metals the prolonged aging caused the reduction of the amount of ferrite (δ), which confirms the microstructural aspects observed in Figures 6(a) and (b), i.e., the decomposition of ferrite phase. It can be inferred that, due to the high Cr content, the α' precipitates are less ferromagnetic regions, and during the spinodal decomposition process the amplitude of Cr content modulation increases. Cr-rich α' precipitates may become paramagnetic at room temperature in the advanced stages of aging¹⁶. As result, the initial magnetic permeability, which is the basis for the ferritoscope measurement, decreases as the spinodal decomposition of ferrite advances.

The Charpy-V impact toughness curves of the weld metals are shown in Figure 8. Note that un-aged WM-FSW showed lower impact toughness than the WM-GTAW. The higher carbide precipitation in WM-FSW, as predicted in Thermocalc® (Table 6) and identified by EBSD (Tables 9 and 10), may be an explanation for this behavior. The aging at 450°C makes the toughness of both weld metals decrease, but is more pronounced in the GTAW weld metal, probably due to its higher delta ferrite content. As reported^{2,17}, the α' precipitation from the ferrite decomposition precipitation is a strong embrittlement phenomena.

Figures 9(a) and (b) show the fracture surfaces of the weld metals in the as welded conditions. In the WM-GTAW (Figure 9(a)) the fracture surface is characterized by rounded dimples typical of ductile fracture. In WM-FSW the presence of areas of small dimples and secondary cracks are observed, indicating some embrittlement. Figure 10 (a) shows that the WM-GTAW presented a brittle fracture, due to the presence of microvoids ("dimples"), rounded and tearing. Figure 10(b) shows the detail of a fractured ferrite island, possibly caused by the α' phase precipitation.

The variation of pitting potentials obtained by the cyclic potentiodynamic tests is shown in Figure 11. It is observed that in the as welded condition the WM-FSW presents pitting potential (EPITE) superior to the WM-GTAW, as shown in Fig. 12. Although the high EPit value is coincident with the potential of oxygen evolution, the polarization curve showed the hysteresis loop which is characteristic of pit formation, and some pits were also observed in the specimen. Both weld metals contain traces of intermetallic phases and carbides, but the GTAW weld metal seems to be more affected. The higher δ ferrite content of WM-GTAW may also contribute its lower localized corrosion resistance. It is expected that the aging process causes the decrease of pitting resistance. It was clearly observed in the FSW welds, but in the GTAW welds there was an increase of pitting potential after 300 and 400 h of aging. The lower corrosion resistance of FSW after aging for 200h and 300h can also be explained by its fine

grained structure. Some studies^{18,19} suggest that refining of the austenitic grain decreases the pitting corrosion resistance due to the increased diffusion efficiency of Cr and Mo, which favors the intermetallic precipitation during aging.

4. Conclusions

The present study aimed to characterize the welding metals resulting from GTAW and FSW processes in AISI 317L austenitic stainless steel, as well as to evaluate the effect of aging at 450°C for periods of up to 400 hours. The main conclusions are:

- The microstructure of un-aged weld metal of GTAW is characterized by a dendritic structure of austenite, 7.0% of delta ferrite, and small amounts of intermetallic phases (σ and χ) precipitated in the ferrite. Traces of $M_{23}C_6$ carbides were also identified by EBSD analysis. The FSW weld metal contains a microstructure of wrought product with fine grains of austenite, 3.0% of delta ferrite, traces of σ phase, and more carbides and χ phase than the GTAW weld metal.
- The deformation and recrystallization favor the precipitation of intermetallic phases in the un-aged WM-FSW.
- The increase of the exposure time triggered a progressive decomposition of delta ferrite.
- Both FSW and GTAW weld metals suffered embrittlement and pitting corrosion decay due to aging at 450°C.

5. Acknowledgements

The authors thank the Institutions for the support provided in the execution of the present work: To the INT by the experimental support; CAPES, CNPq for financial support and LNNANO for support in the realization of welding.

6. References

1. Plaut RL, Herrera C, Escriba DM, Rios PR, Padilha AF. A short review on wrought austenitic stainless steels at high temperatures: processing, microstructure, properties and performance. *Materials Research*. 2007;10(4):453-460.
2. Lo KH, Shek CH, Lai JKL. Recent developments in stainless steels. *Materials Science and Engineering: R: Reports*. 2009;65(4-6):39-104.
3. Silva CC, Miranda HC, Sant'Ana HB, Farias JP. Microstructure, hardness and petroleum corrosion evaluation of 316L/AWS E309MoL-16 weld metal. *Materials Characterization*. 2009;60(4):346-352.
4. Khatak HS, Raj B, eds. *Corrosion of Austenitic Stainless Steels: Mechanism, Mitigation and Monitoring*. Cambridge: Woodhead Publishing; 2002.

5. Unnikrishnan R, Satish Idury KSN, Ismail TP, Bhadauria A, Shekhawat SK, Khatirkar RK, et al. Effect of heat input on the microstructure, residual stresses and corrosion resistance of 304L austenitic stainless steel weldments. *Materials Characterization*. 2014;93:10-23.
6. Chun EJ, Baba H, Terashima K, Nishimoto K, Saida K. Prediction of σ -Phase Embrittlement in Type 316FR Weld Metal. *Welding Journal*. 2013;92(Suppl):133s-139s.
7. American Welding Society. *C5.5-80 - Recommended Practices for Gas Tungsten Arc Welding*. Miami: American Welding Society; 1980.
8. Wei LY, Nelson TW. Correlation of Microstructures and Process Variables in FSW HSLA-65 Steel. *Welding Journal*. 2011;90(Suppl):95s-101s.
9. ASTM International. *ASTM G61-86 - Standard Test Method for Conducting Cyclic Potentiodynamic Polarization Measurements for Localized Corrosion Susceptibility of Iron-, Nickel-, or Cobalt-Based Alloys*. West Conshohocken: ASTM International; 2009.
10. Lippold JC, Kotecki DJ. *Welding Metallurgy and Weldability of Stainless Steels*. Hoboken: John Willey & Sons; 2005.
11. Song Y, Baker TN, McPherson NA. A study of precipitation in as-welded 316LN plate using 316L/317L weld metal. *Materials Science & Engineering: A*. 1996;212(2):228-234.
12. Park SHC, Sato YS, Kokawa H, Okamoto K, Hirano S, Inagaki M. Rapid formation of the sigma phase in 304 stainless steel during friction stir welding. *Scripta Materialia*. 2003;49(12):1175-1180.
13. Kokawa H, Park SHC, Sato YS, Okamoto K, Hirano S, Inagaki M. Microstructure in Friction Stir Welded 304 Austenitic Stainless Steel. *Welding in The World*. 2005;49(3-4):34-40.
14. Chen YC, Fujii H, Tsumura T, Kitagawa Y, Nakata K, Ikeuchi K, et al. Banded structure and its distribution in friction stir processing of 316L austenitic stainless steel. *Journal of Nuclear Materials*. 2012;420(1-3):497-500.
15. ASTM International. *ASTM E112-13 - Standard Test Methods for Determining Average Grain Size*. West Conshohocken: ASTM International; 2013.
16. Tavares SSM, Da Silva MR, Neto JM. Magnetic properties changes during embrittlement of a duplex stainless steel. *Journal of Alloys and Compounds*. 2000;313(1-2):168-173.
17. Totten GE, ed. *Steel Heat Treatment: Metallurgy and Technologies*. Boca Raton: CRC Press; 2006.
18. Ralston KD, Birbilis N. Effect of Grain Size on Corrosion: A Review. *Corrosion*. 2010;66(7):075005-075005-13.
19. Xin SS, Xu J, Lang FJ, Li MC. Effect of Temperature and Grain Size on the Corrosion Behavior of 316L Stainless Steel in Seawater. *Advanced Materials Research*. 2011;299-300:175-178.